frontiers | Frontiers in Mechanical Engineering

ORIGINAL RESEARCH
published: 28 April 2022
doi: 10.3389/fmech.2022.876655

Zintl Phase Compounds $Mg_3Sb_{2-x}Bi_x$ (x = 0, 1, and 2) Monolayers: Electronic, Phonon and Thermoelectric Properties From ab Initio Calculations

Zheng Chang[1], Jing Ma[1], Kunpeng Yuan[1], Jiongzhi Zheng[2], Bin Wei[3], Mohammed Al-Fahdi[4], Yufei Gao[1], Xiaoliang Zhang[1], Hezhu Shao[5]*, Ming Hu[4]* and Dawei Tang[1]**

[1]Key Laboratory of Ocean Energy Utilization and Energy Conservation of Ministry of Education, School of Energy and Power Engineering, Dalian University of Technology, Dalian, China, [2]Department of Mechanical and Aerospace Engineering, The Hong Kong University of Science and Technology, Hong Kong, China, [3]Henan Key Laboratory of Materials on Deep-Earth Engineering, School of Materials Science and Engineering, Henan Polytechnic University, Jiaozuo, China, [4]Department of Mechanical Engineering, University of South Carolina, Columbia, SC, United States, [5]College of Electrical and Electronic Engineering, Wenzhou University, Wenzhou, China

OPEN ACCESS

Edited by:
Yaguo Wang,
University of Texas at Austin,
United States

Reviewed by:
Shangchao Lin,
Shanghai Jiao Tong University, China
Xiangjun Liu,
Donghua University, China

***Correspondence:**
Xiaoliang Zhang
zhangxiaoliang@dlut.edu.cn
Hezhu Shao
hzshao@wzu.edu.cn
Ming Hu
hu@sc.edu
Dawei Tang
dwtang@dlut.edu.cn

Specialty section:
This article was submitted to Thermal and Mass Transport, a section of the journal Frontiers in Mechanical Engineering

Received: 15 February 2022
Accepted: 22 March 2022
Published: 28 April 2022

Citation:
Chang Z, Ma J, Yuan K, Zheng J, Wei B, Al-Fahdi M, Gao Y, Zhang X, Shao H, Hu M and Tang D (2022) Zintl Phase Compounds $Mg_3Sb_{2-x}Bi_x$ (x = 0, 1, and 2) Monolayers: Electronic, Phonon and Thermoelectric Properties From ab Initio Calculations. Front. Mech. Eng 8:876655. doi: 10.3389/fmech.2022.876655

The $Mg_3Sb_{2-x}Bi_x$ family has emerged as the potential candidates for thermoelectric applications due to their ultra-low lattice thermal conductivity (κ_L) at room temperature (RT) and structural complexity. Here, using ab initio calculations of the electron-phonon averaged (EPA) approximation coupled with Boltzmann transport equation (BTE), we have studied electronic, phonon and thermoelectric properties of $Mg_3Sb_{2-x}Bi_x$ (x = 0, 1, and 2) monolayers. In violation of common mass-trend expectations, increasing Bi element content with heavier Zintl phase compounds yields an abnormal change in κ_L in two-dimensional $Mg_3Sb_{2-x}Bi_x$ crystals at RT (~0.51, 1.86, and 0.25 W/mK for Mg_3Sb_2, Mg_3SbBi, and Mg_3Bi_2). The κ_L trend was detailedly analyzed via the phonon heat capacity, group velocity and lifetime parameters. Based on quantitative electronic band structures, the electronic bonding through the crystal orbital Hamilton population (COHP) and electron local function analysis we reveal the underlying mechanism for the semiconductor-semimetallic transition of $Mg_3Sb_{2-x}Bi_x$ compounds, and these electronic transport properties (Seebeck coefficient, electrical conductivity, and electronic thermal conductivity) were calculated. We demonstrate that the highest dimensionless figure of merit ZT of $Mg_3Sb_{2-x}Bi_x$ compounds with increasing Bi content can reach ~1.6, 0.2, and 0.6 at 700 K, respectively. Our results can indicate that replacing heavier anion element in Zintl phase $Mg_3Sb_{2-x}Bi_x$ materials go beyond common expectations (a heavier atom always lead to a lower κ_L from Slack's theory), which provide a novel insight for regulating thermoelectric performance without restricting conventional heavy atomic mass approach.

Keywords: two-dimensional zintl phase compounds, phonon thermal transport, thermoelectric performance, electron-phonon averaged approximation, Boltzmann transport equation

INTRODUCTION

The term Zintl phase was firstly proposed by F. Laves (Kauzlarich et al., 2007; Kauzlarich et al., 2016), as a German scientist, indicating a collection of materials within the general class of intermetallics, and the compounds can be understood by a formal electron transfer from a positively-charged metal to a negatively-charged element. In particular, the rich chemistry and evolution of structural complexity of Zintl phase compounds become a series of promising thermoelectric (TE) materials because of their "phonon-glass electron-crystal (PGEC)" (Shuai et al., 2017; Rowe, 2018) structures. The ideal concept presents that a high-performance TE material should have an excellent electrical conductivity of crystals, but also have a higher phonon-scattering rate like glass, where the cation region act as "phonon-glass" and the anion region play as "electron crystal" to alter phonon thermal and electrical transport properties. More interestingly, the structural complexity of Zintl phase compounds is mainly manifested in the diversity of anionic frameworks composed of internal covalent bonds, and the anionic framework can be roughly divided into zero-dimensional (0D) cluster, one-dimensional (1D) chain, two-dimensional (2D) planar, and complex three-dimensional (3D) network structures in accordance with the spatial extension. The 0D cluster structures include Sr_3AlSb_3 (Zevalkink et al., 2013) and $Yb_{14}MnSb_{11}$ (Brown et al., 2006), and $Yb_{14}MnSb_{11}$ in the high temperature region can reach 1, in which the maximum Seebeck coefficient of Sr_3AlSb_3 is 500 μV K^{-1} in the medium temperature region. Herein, the figure of merit defined as ZT ($ZT = \sigma S^2 T/(\kappa_e + \kappa_L)$), where σ stands for the electrical conductivity, S represents the Seebeck coefficient, and T is the Kelvin temperature. κ_e and κ_L are the electronic and the lattice thermal conductivities, respectively. Next, Sr3GaSb3 (Zevalkink et al., 2012) and $A_5Sn_2As_6$ (A = Sr and Eu) (Wang et al., 2012) represent the 1D chain structures, where the maximum ZT of Sr_3TGaSb_3 at 1000 K can exceed 0.9 by doping with Zn element. Meanwhile, the 2D planar structures incorporate $BaGa_2Pn_2$ (A = P, As) (He et al., 2010) and $YbGd_2Sb_2$ (Xia and Bobev, 2007). The representative of the 3D network structures is skutterudite (CoSb3) (Shi et al., 2005; Liu et al., 2020), which is a near-ideal "PGEC" with the higher S (200 μV K^{-1}) and power factor (σS^2) (30 μW cm^{-1} K^{-1}), while the higher lattice thermal conductivity would suppress its TE performance.

Recently, the $Mg_3Sb_{2-x}Bi_x$ compounds have become one of the most widely studied TE materials owing to their abundant and inexpensive constituent elements. Experimental measurements and theoretical calculations suggested that the ZT of Mg_3Sb_2 can reach 1 in the high temperature region, and it has simple synthesis, a high melting point, and excellent mechanical stability (Ohno et al., 2018; Shi et al., 2018). It is worth noting that $Mg_3(SbBi)_2$ alloys would reduce the effective mass of Mg_3Sb_2 and further help to increase the carrier mobility (Imasato et al., 2018). Meanwhile, it was reported that increasing the Bi content in N-type $Mg_3Sb_{2-x}Bi_x$ compounds can significantly improve the low-temperature ZT value (Imasato et al., 2018; Shu et al., 2019), which is even comparable to N-type Bi_2Te_3. However, it was designed and shown that a ZT of 1.85 for $Mg_{3.195}Mn_{0.05}Sb_{1.5}Bi_{0.49}Te_{0.01}$ at 723 K can reach 1.85 (Chen et al., 2018), which is still lower than that of a class of superior TE materials such as SnSe (~2.8 at 773 K) (Zhao et al., 2014; Zhao et al., 2016; Chang et al., 2018). The above studies mainly focus on the TE transport properties of 3D Zintl phase $Mg_3Sb_{2-x}Bi_x$ (x = 0, 1, and 2) family. According to the 2D quantum confinement effect (Hicks and Dresselhaus, 1993; Zeng et al., 2018), we know that decreasing dimension in 3D materials can not only reduce the κ_L but also avoid appearing the poor TE performance in some crystalline orientations. The previous work suggested that the ZT value of 2D Mg_3Sb_2 can increase to 2.5 at 900 K, and the near record-high value is larger than that of 3D structure (Huang et al., 2019). The TE performance of 3D Zintl phase $Mg_3Sb_{2-x}Bi_x$ compounds, as a typical layered TE materials family, may be further enhanced through the dimensionality reduction approach. Yet, few 2D Zintl phase $Mg_3Sb_{2-x}Bi_x$ compounds have been studied, and it is necessary to further explore the behind mechanism for the excellent TE performance.

In this work, we performed the first-principles calculations combining with the BTE and the EPA approximation (as a more predictive approach than the deformation potential approximation method) (Samsonidze and Kozinsky, 2018) to systematically calculate and detailedly analyze the phonon thermal and TE transport properties of 2D $Mg_3Sb_{2-x}Bi_x$ within a wide range of temperature. It is found that, through our theoretical calculations, 2D $Mg_3Sb_{2-x}Bi_x$ (x = 0, 1, and 2) compounds possess an abnormal κ_L trend ($\kappa_L^{Mg_3SbBi} > \kappa_L^{Mg_3Sb_2} > \kappa_L^{Mg_3Bi_2}$), which violates the common theory (Heavier atomic mass in similar materials usually corresponds to lower κ_L). We elucidate the reason why this anomaly occurs in 2D $Mg_3Sb_{2-x}Bi_x$ structures by quantitatively comparing the phonon heat capacity, the phonon group velocities, the phonon lifetime, the anharmonicity, the transferred and shared charge, and the characteristics of bonds. Meanwhile, we further calculated the electrical transport properties in 2D $Mg_3Sb_{2-x}Bi_x$ including the σ, S, κ_e, and TE performance as a function of chemical potential with respect to the Fermi energy under different temperatures. Our results will provide a theoretical basis for accelerating TE application of 2D Zintl phase materials and pave a new way for predicting and exploring the ultra-high TE performance in PGEC family materials.

Computational Details

The phonon thermal and electrical transport properties have been calculated by the plane-wave pseudopotential approach within the density functional theory (DFT) (Hohenberg and Kohn, 1964), which is employed in the Vienna Ab-initio Simulation Package (VASP) (Kresse and Furthmüller, 1996) software along with projector augmented-wave (PAW) potential (Bliichl, 1994). To ensure the good convergence of electrons and ions during structural optimizations, the plane-wave cutoff energy of the 2D $Mg_3Sb_{2-x}Bi_x$ compounds was set as 500 eV, and a Monkhorst-Pack k-point grid of 15 × 15 × 1 was used to ensure accurate calculation. A Hellmann-Feynman force convergence threshold of 10^{-4} eV A^{-1} was adopted, and the energy convergence threshold between the two steps was set to be 10^{-6} eV. To avoid the effect of the interaction between adjacent layers, 2D

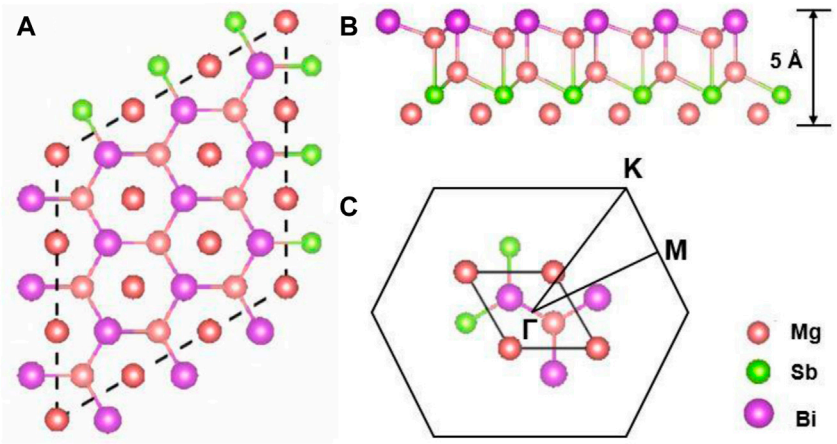

FIGURE 1 | Schematic illustration of 2D $Mg_3Sb_{2-x}Bi_x$ in a 5 × 5 × 1 supercell: **(A)** top view and **(B)** side view; Mg, Sb ,and Bi are represented orange, green and purple, respectively. **(C)** The corresponding primitive cell and the first Brillouin zone path with high-symmetry points in 2D $Mg_3Sb_{2-x}Bi_x$ compounds.

$Mg_3Sb_{2-x}Bi_x$ unit cells were added a 20 Å thickness of vacuum slab along the *out-of-plane* direction. We next calculated the electronic band structures using the Perdew, Burke, and Ernzerhof (PBE) functional (Perdew et al., 1996) and the hybrid Heyd–Scuseria–Ernzerhof (HSE06) functional (Paier et al., 2006), and different functionals are designed to obtain accurate band results for 2D $Mg_3Sb_{2-x}Bi_x$ materials. The κ_L is computed by solving the linearized BTE as implemented in ShengBTE software (Li et al., 2014), then considering Born effective charges and dielectric constants effect in the selected compounds. Meanwhile, electronic transport coefficients are calculated exactly by solving semi-classical BTE within the EPA approximation (fully first-principles computations of electron-phonon interactions) as described detailedly (see **Supplementary material**) in the excellent work (Samsonidze and Kozinsky, 2018).

RESULTS AND DISCUSSIONS

Herein, 2D $Mg_3Sb_{2-x}Bi_x$ (x = 0, 1, and 2) compounds belong to a typical hexagonal structure with the space group *P*3*m*1 (No. 156) which is made up of the cationic layer of Mg^{2+} and the anionic layer of $[Mg_2(Sb_{2-x}Bi_x)]^{2-}$ as shown in **Figure 1**. It has been found that the bonds between ionic Mg^{2+} layers and covalent $[Mg_2(Sb_{2-x}Bi_x)]^{2-}$ layers can be broken to produce a corresponding 2D materials (Gorai et al., 2016; Zhang et al., 2018). **Figures 1A, B** represents schematic illustration of 2D $Mg_3Sb_{2-x}Bi_x$ (x = 0, 1, and 2), and their calculated lattice constants within the PBE-level are 4.736 Å, 4.794 Å, and 4.843 Å, respectively, which are close to the lattice parameters for corresponding 3D Mg_3Sb_2 (4.573 Å) (Huang et al., 2019) and 3D Mg_3Bi_2 (4.666 Å) (Zhang and Iversen, 2019). Meanwhile, during the structural relaxation of 2D $Mg_3Sb_{2-x}Bi_x$, we did not consider the too weak van der Waals effect, which has been reported and investigated in previous work (Zhang et al., 2018). Meanwhile, we also present the first Brillouin zone path (Γ-M-K-Γ) with high-symmetry points, named Γ (0, 0, 0), M (1/2, 0, 0), and K (1/3, 1/3, 0), as illustrated in **Figure 1C**. It is obviously seen that two cases of Mg atoms exist in the primitive cell of 2D $Mg_3Sb_{2-x}Bi_x$, named by Mg1 and Mg2 (see the inset of the **Figures 2B, D, F**. Interestingly, between Mg and Sb atoms interactions caused by the corresponding electrical properties has been confirmed, which can occur in a Mg-Sb bonding interaction for the all Mg1 and Mg2 cases in N-type doping Mg_3Sb_2 (Sun et al., 2019). Therefore, it should be noted that the bonding characteristic in 2D $Mg_3Sb_{2-x}Bi_x$ compounds may directly determine their electronic and phononic structures and thus play a crucial role in the calculations of TE properties.

The 2D $Mg_3Sb_{2-x}Bi_x$ family has five atoms in the primitive cell, and the corresponding phonon dispersion curves and phonon harmonicity results are depicted in **Figure 2**. We found that the above compounds have not imaginary vibrational frequency in the phonon dispersion curves, indicating the dynamic stability of the 2D $Mg_3Sb_{2-x}Bi_x$ compounds in this study (Chang et al., 2021). Meanwhile, it can be seen from **Figure 2** that the mixing of acoustic phonons and low-frequency optical phonons exist a stronger phonon scattering processes, which indicates a lower κ_L in these materials. From **Figures 2A, C, F**, it can be clearly observed that the region of colored phonon band-gap (Significant dispersion in the high-frequency optical phonons) are gradually decreased with increasing Bi atom content, and these optical phonons in the current compounds holds non-zero phonon group velocities and then has a certain contribution to phonon heat transport. We further track the phenomenon by comparing atom-projected phonon DOS of the Mg, Sb, and Bi atoms in these related compounds, as depicted in **Figures 2A, C, E**. The total phonon DOS of Mg_3Sb_2 and Mg_3SbBi monolayers decomposes into two separate regions: Mg-site mainly dominated between 6 and 9 THz, and Sb/Bi-sites mainly dominated below ~3 THz. Surprisingly, for Mg_3Bi_2 monolayer, the total phonon DOS decomposes into three separate regions: Mg1-site mainly dominated between 6 and 8 THz, Mg2-site mainly dominated between 2 and five THz, and Bi-sites mainly dominated below

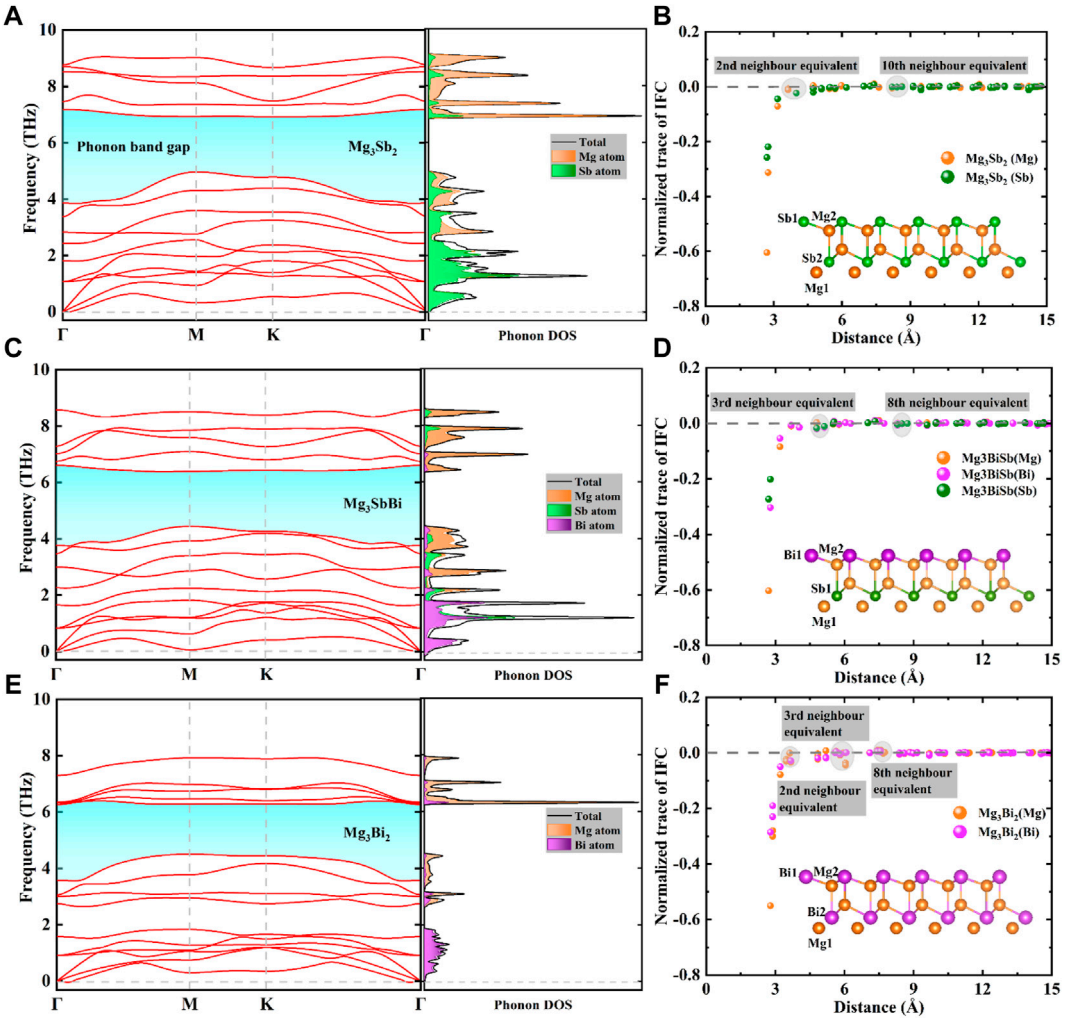

FIGURE 2 | Calculated phonon dispersion curves and atom-projected density of states (DOS) for **(A)** 2D Mg_3Sb_2, **(C)** 2D Mg_3SbBi and **(E)** 2D Mg_3Bi_2. The colored shapes highlight phonon band gaps in these compounds. Normalized trace of interatomic force constant (IFC) tensors as a function of atomic distances of **(B)** 2D Mg_3Sb_2, **(D)** 2D Mg_3SbBi and **(F)** 2D Mg_3Bi_2, respectively.

~2 THz. The above results show that all of phonon vibration frequencies would be more compressed with increasing Bi atomic mass, which benefits for becoming high-performance TE materials, while it is not enough to explain the anomalous κ_L changes in 2D $Mg_3Sb_{2-x}Bi_x$ compounds by the increased Bi atomic mass. Therefore, it is urgent to study the interatomic force constants (IFCs) effect in $Mg_3Sb_{2-x}Bi_x$ family, which can directly determine phonon heat conduction behavior.

Figures 2B, D, F show the presence of long-ranged interaction among these compounds, and to further compare and analyze the IFCs between Mg atom and Sb/Bi atoms, traces of IFC tensors are normalized by the trace values of the self-interacting IFC tensor in the above compounds. For instance, second-nearest neighbours, separated by ~4 Å (including Mg1-Sb1, Mg1-Sb2, and Mg1-Mg2, etc.,), have interactions that are comparable to those of tenth-nearest neighbours, spaced ~9 Å apart, and much weaker than first-neighbours interactions in **Figure 2B**. Clearly, there are very similar phenomenon for normalized trace of IFC in 2D Mg_3SbBi and Mg_3Bi_2 structures, excepting for the reduced distances at same nearest neighbours cases by the increased Bi content. Herein, we calculate the IFC tensor on the basis of first-principles calculations as follow (Lee et al., 2014; Li et al., 2020a; Li et al., 2020b):

$$\frac{\partial^2 E}{\partial R_I \partial R_J} = \begin{bmatrix} \frac{\partial^2 E}{\partial R_x \partial R_x} & \frac{\partial^2 E}{\partial R_x \partial R_y} & \frac{\partial^2 E}{\partial R_x \partial R_z} \\ \frac{\partial^2 E}{\partial R_y \partial R_x} & \frac{\partial^2 E}{\partial R_y \partial R_y} & \frac{\partial^2 E}{\partial R_y \partial R_z} \\ \frac{\partial^2 E}{\partial R_z \partial R_x} & \frac{\partial^2 E}{\partial R_z \partial R_y} & \frac{\partial^2 E}{\partial R_z \partial R_z} \end{bmatrix}, \quad (1)$$

where E and R_α represent energy and atomic position along α direction, respectively. By computing the trace of IFC tensors, we

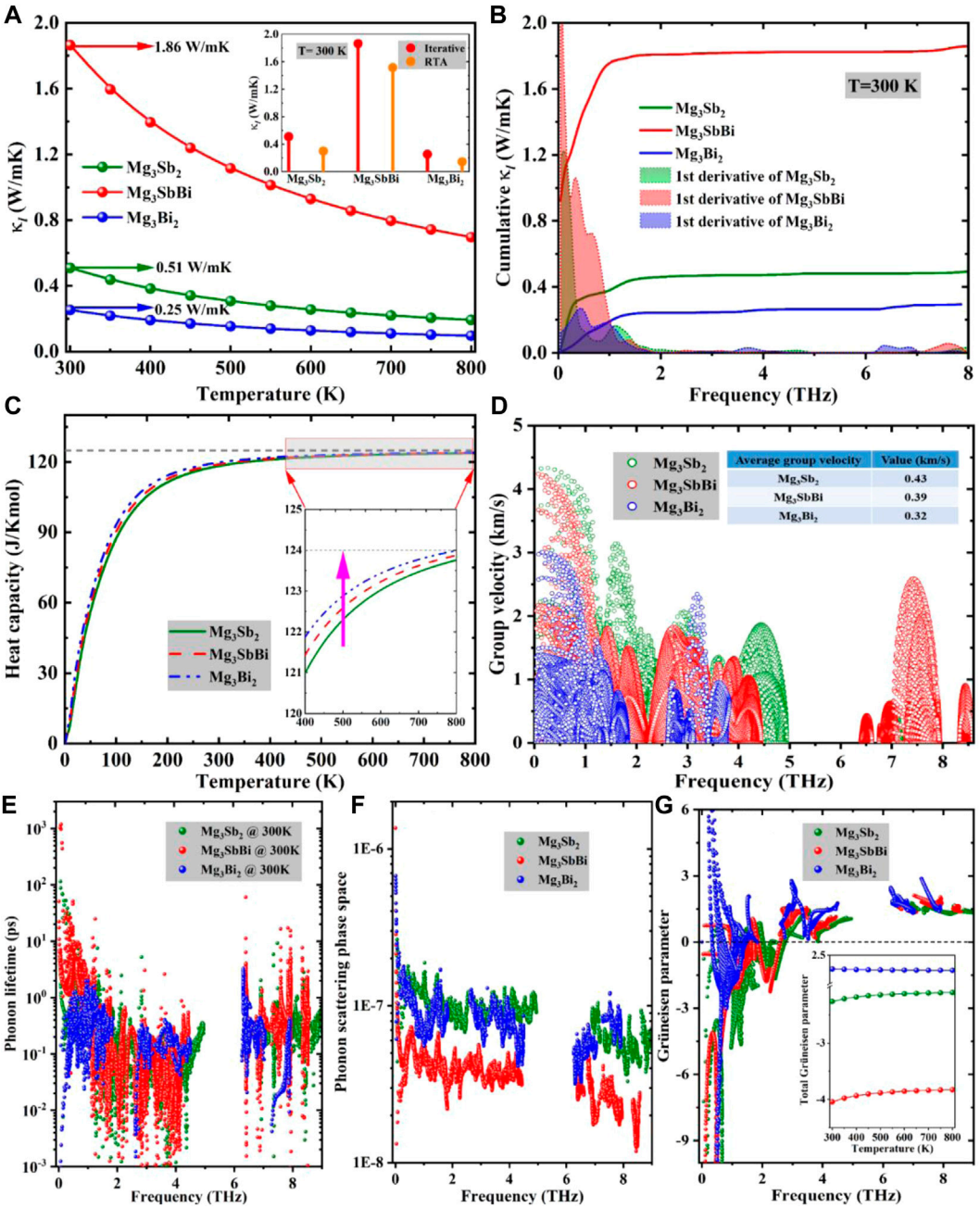

FIGURE 3 | (A) Calculated κ_L of 2D $Mg_3Sb_{2-x}Bi_x$ with respect to the temperature ranging from 300 to 800 K. **(B)** Cumulative κ_L of these compounds and their derivatives versus phonon frequency at 300 K. **(C)** Calculated changes of phonon heat capacity of the above compounds as a function of temperature. The phonon frequency-dependent behavior of **(D)** the phonon group velocities, **(E)** phonon lifetime, **(F)** phonon scattering phase space, and **(G)** Grüneisen parameters in 2D $Mg_3Sb_{2-x}Bi_x$.

can assess bonding stiffness regardless of crystal structure or coordinate system:

$$Trace\ of\ IFC = \frac{\partial^2 E}{\partial R_x \partial R_x} + \frac{\partial^2 E}{\partial R_y \partial R_y} + \frac{\partial^2 E}{\partial R_z \partial R_z}, \quad (2)$$

Finally, the normalization is calculated by the trace value of self-interaction force constants:

$$Normalized\ trace\ of\ IFC = \frac{\frac{\partial^2 E}{\partial R_{0,x} \partial R_{n,x}} + \frac{\partial^2 E}{\partial R_{0,y} \partial R_{n,y}} + \frac{\partial^2 E}{\partial R_{0,z} \partial R_{n,z}}}{\frac{\partial^2 E}{\partial R_{0,x} \partial R_{0,x}} + \frac{\partial^2 E}{\partial R_{0,y} \partial R_{0,y}} + \frac{\partial^2 E}{\partial R_{0,z} \partial R_{0,z}}}. \quad (3)$$

In addition, to describe accurately the related IFCs in the calculation of κ_L, we choose a cutoff distance of the tenth-nearest neighbor in 2D $Mg_3Sb_{2-x}Bi_x$ family. We need to point out that

Mg1 atom exists at the octahedral site surrounded by 6 corresponding atoms, which would provide 2 electrons to the $[Mg_2(Sb_{2-x}Bi_x)]^{2-}$ network, while Mg2 atom exists at the tetrahedral site surrounded by 4 corresponding atoms. In terms of its configuration, a detailed chemical bonding analysis of 3D Mg_3Sb_2 has been reported that the two different Mg atom sites present a similar bonding character responding to the transferred charges of +1.51 and +1.47, respectively (Zhang et al., 2019), and exists dominantly ionic bonds with partial covalent bonds in 3D Mg_3Sb_2 system (Zhang et al., 2018). These results offers a rational explanation of the relation to phonon heat conduction properties of 3D $Mg_3Sb_{2-x}Bi_x$ family. To deeply understand bonding character and quantify the bond hierarchy strengths of a pair of atoms in 2D $Mg_3Sb_{2-x}Bi_x$ compounds, we next compute and analyze the transferred and shared charges and COHP along with integrated "-COHP" (ICOHP) for the nearest-neighbor atom in the following section.

Based on the more accurate second- and third-order IFCs from the normalized trace of IFC data, we firstly calculate the κ_L of the selected three Zintl-phase compounds as shown in **Figure 3A**. Each material would demonstrate roughly the common $\kappa_L \sim 1/T$ behavior. Meanwhile, it is well known that the calculation of κ_L is more sensitive to the selection of q-mesh grids, and we set a q-mesh grid of $100 \times 100 \times 1$ to solve phonon BTE and then obtain the convergence of κ_L. Because of the symmetry of 2D $Mg_3Sb_{2-x}Bi_x$, the κ_L along two in-plane directions shows isotropy, so only a value are depicted. As seen from **Figure 3A** , 2D Mg_3SbBi alloy holds a higher lattice thermal conductivity, while its average atomic mass is between those of 2D Mg_3Sb_2 and 2D Mg_3Bi_2. For instance, our calculated κ_L of Mg_3Sb_2, Mg_3SbBi, and Mg_3Bi_2 monolayers at 300 K are 0.51, 1.86, and 0.25 W/mK, respectively, which may originate from a smaller displacement and the mass difference (related to bonding strength) caused by a heavier atom (Li and Mingo, 2014; Yang et al., 2020). As presented in the inset of **Figure 3A**, we further study the κ_L changes between the relaxation time approximation (RTA) and the iteratively solving (ITE) methods among the three materials, and the RTA results are below the ITE data, indicating the main function of the Umklapp processes in phonon heat conduction behavior. To deeply understand the behind mechanism of the intriguing phenomena, we perform a detailed analysis on phonon frequency-dependent cumulative κ_L, decomposing κ_L to three separate parts (phonon heat capacity, group velocity, and phonon lifetime), and phonon anharmonicity information, as presented in **Figures 3B–G**.

Obviously, with the increase of cumulative κ_L can become negligible above a frequency value of ~2 THz among the three 2D Zintl phase compounds, suggesting the major contribution of the lower optical and acoustic phonons to κ_L (**Figure 2**). What we need to notice is that 2D Mg_3SbBi and 2D Mg_3Bi_2 exist two relatively small shape areas (blue and red marked) between 6 and 8 THz, because the higher optical phonons would be compressed and then benefit three-phonon scattering processes. To further check the contribution of all phonons vibrations to the calculated κ_L, the phonon heat capacity (C_v) of among 2D Mg_3Sb_2, 2D Mg_3SbBi and 2D Mg_3Bi_2 with respect to temperature were obtained and illustrated in **Figure 3B**, which agree well with the previous experimental data by using the PPMS measurement (Xin et al., 2018). The C_v (obeying $\kappa_L \propto C_v$) of these compounds at temperatures within the range of 400–800 K are very close (~122 J/K mol) to each other for all the three materials, and obey the classical limit of Dulong-Petit law (Fitzgerel and Verhoek, 1960) as shown in the inset of **Figure 3C**. Therefore, these tiny difference in C_v are not the primary cause of the anomalous κ_L trend in 2D $Mg_3Sb_{2-x}Bi_x$ systems. For three compounds, the phonon group velocity (v_g) as a function of frequency is plotted in **Figure 3D**, and it can be seen that the group velocity of 2D Mg_3Sb_2 is higher than that of 2D Mg_3Bi_2, closing to that of 2D Mg_3SbBi in the cutoff frequency below 1.5 THz, which suggests the calculated κ_L of 2D Mg_3Sb_2 and 2D Mg_3SbBi might be roughly close (following the rule $\kappa_L \propto v_g$). On average level, we show that the average group velocities of 2D $Mg_3Sb_{2-x}Bi_x$ are 0.43, 0.39, and 0.32 km/s, respectively. However, it is clearly observed in **Figure 3D** that the three v_g data exist similar distribution, excepting for having the significant differences (the non-negligible velocities for Mg_3SbBi) around a frequency ranging between 6.5 and 8 THz, while the changes are consistent with the above the slope of phonon dispersion curves.

Interestingly, none of the C_v and the v_g can explain the relatively higher κ_L of 2D Mg_3SbBi compared to 2D Mg_3Sb_2 systems. Therefore, we can conclude that the abnormal κ_L trends in the three materials must lie in the unusual phonon lifetimes (τ) as plotted in **Figure 3E**. The calculated τ of 2D Mg_3SbBi were considerably larger than those of the other two materials in the lower- (0–2 THz) and higher-frequency (6–8 THz) regions, which might be because of the suppressed three-phonon scattering processes in 2D Mg_3SbBi, caused by the alloying (a mass difference occurring in $[Mg_2(SbBi)]^{2-}$). Obviously, these variation trends of the τ in $Mg_3Sb_{2-x}Bi_x$ were consistent with the cumulative κ_L results as seen in **Figure 3B**. In the light of the theory of lattice dynamics, the calculated τ is strongly dependent on three-phonon scattering phase space (P_3) and Grüneisen parameter (γ), as presented in **Figures 3F, G**. Herein, the P_3 is defined as (Lindsay and Broido, 2008; Peng et al., 2016; Yang et al., 2020):

$$P_3 = \frac{2}{3\Theta}\left(P_3^+ + \frac{1}{2}P_3^-\right), \tag{4}$$

$$P_3^{\pm} = \sum_{\lambda} \int d\boldsymbol{q} D_{\lambda}^{\pm}(\boldsymbol{q}), \tag{5}$$

$$D_{\lambda}^{\pm}(\boldsymbol{q}) = \sum_{\lambda'\lambda''} \int d\boldsymbol{q}' \delta\left(\omega_{\lambda}(\boldsymbol{q}) \pm \omega_{\lambda'}(\boldsymbol{q}') - \omega_{\lambda''}\left(\boldsymbol{q} \pm \boldsymbol{q}'' - \boldsymbol{G}\right)\right), \tag{6}$$

where Θ represents a normalization factor, $D_{\lambda}^{\pm}(\boldsymbol{q})$ represents two types of three-phonon scattering channels, and it is also the two phonon DOS and momentum conservation were imposed on $\boldsymbol{q}''$ (Okubo and Tamura, 1983). From **Figure 3F**, it is shown that the P_3 of 2D Mg_3SbBi is smaller than these of the other two compounds in the entire phonon frequency ranges, which suggests that phonons in 2D Mg_3SbBi have less phonon scattering channels, leading to relatively larger τ (**Figure 3E**) compared to 2D Mg_3Sb_2 and 2D Mg_3Bi_2 materials. The other important factor that the number of phonons scattering

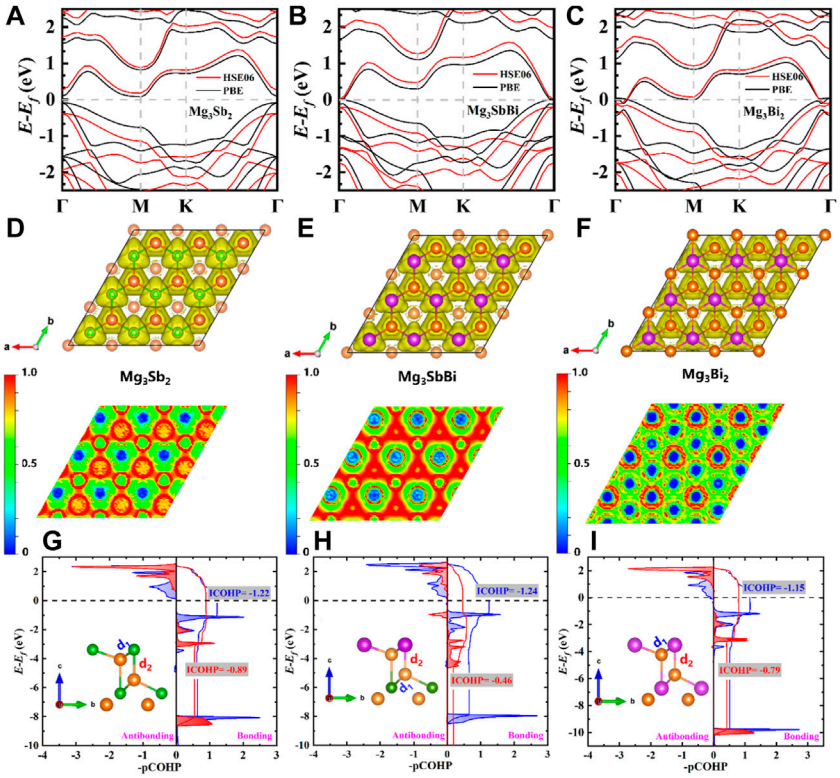

FIGURE 4 | Calculated electronic band structures of **(A)** 2D Mg_3Sb_2, **(B)** 2D Mg_3SbBi, and **(C)** 2D Mg_3Bi_2 by using HSE06 (solid red lines) and PBE function potentials (solid black lines), and the Fermi-level (E_f) is set to 0 eV. Top view (upper) and the corresponding slice projection along (001) plane (down) of 2D $Mg_3Sb_{2-x}Bi_x$ electron localization function (ELF) for **(D)** 2D Mg_3Sb_2, **(E)** 2D Mg_3SbBi, and **(F)** 2D Mg_3Bi_2, respectively. Calculated the projected Crystal Orbital Hamilton Population (pCOHP) curves of 2D $Mg_3Sb_{2-x}Bi_x$ pairwise interactions (including d_1 and d_2) *versus* energy for **(G)** 2D Mg_3Sb_2, **(H)** 2D Mg_3SbBi, and **(I)** 2D Mg_3Bi_2. Herein, the bond behind mechanism of both d_1 and d_2 was investigated and studied by the standalone computer program Local Orbital Basis Suite towards Electronic-Structure Reconstruction (LOBSTER) program (Maintz et al., 2016).

channels determined exists the strength of phonon anharmonicity, quantitatively described by the γ, which characterizes how many phonon frequencies vary with the crystal volume. As revealed in the inset of **Figure 3G**, the calculated total γ for 2D Mg_3SbBi is ~ −4.0, which is lower than that of 2D Mg_3Sb_2 (γ= ~ −2.1) and 2D Mg_3Bi_2 (γ= ~ 2.2) at the temperature ranging from 300 to 800 K. Consequently, anomalously increase of the κ_L from 2D Mg_3Sb_2, 2D Mg_3SbBi, and 2D Mg_3Bi_2 has been demonstrated by breaking up into the relative contribution of the C_v, v_g, and τ as discussed above.

It is well known that the superior TE performance in a material results from an intrinsic ultra-low κ_L, from the above phonon heat conduction results, and it is very necessary to confirm the potential TE transport properties from 2D Mg_3Sb_2 to 2D Mg_3Bi_2. We firstly calculated the electronic band structures in 2D $Mg_3Sb_{2-x}Bi_x$ using the two function potentials as plotted in **Figures 4A–C**, which can directly explain the reason for the high TE performance of a material. Since Sb and Bi atoms possessed the same outermost valence electrons (including 3*p* and 2*s*), the slope of these band structures would be very similar. Meanwhile, the calculated band-gaps with PBE and HSE06 potentials are 0.17 and 0.56 eV for 2D Mg_3Sb_2. Therefore, to obtain more accurate values, we carried out the HSE06 to correct the band structures, and a negative band-gap was occurred in 2D Mg_3Bi_2 (**Figure 4C**). In addition, we found that the valence band maximum is located at Γ point for all of the selected compounds, due to the domination of Mg-Sb/Bi bonding interactions (Sun et al., 2019; Wood et al., 2020), while location of the conduction band minimum are between Γ and M paths, the same Γ point, and around Γ point for 2D Mg_3Sb_2, 2D Mg_3SbBi, and 2D Mg_3Bi_2, respectively. To further characterize and explore the behind mechanism of chemical-bonding properties in 2D $Mg_3Sb_{2-x}Bi_x$, we also calculated the ELF and COHP with integrated pCOHP (-pCOHP) as plotted in **Figures 4D–I**. Meanwhile, three ELF values of 0, 0.5, and 1.0 reflect non-localized electrons (none-charge density), completely delocalized electrons (electron gas–like pair phenomenon), and fully localized electrons (the occurrence probability of the electrons), respectively (Silvi and Savin, 1994; Yue et al., 2017; Wu et al., 2020). It can be clearly seen that the value of the ELF between Mg atoms and Sb/Bi atoms gradually decrease with increasing Bi element in 2D $Mg_3Sb_{2-x}Bi_x$ systems, suggesting a weaker covalent bond in 2D Mg_3Bi_2 and then proved its semi-metallic feature. The lower value of ELF in Mg_3Bi_2 monolayer also confirms the weaker and lower shared charges as listed in

TABLE 1 | Comparison of transferred and shared charges (|e|) and the corresponding transferred charge (|e|) of each element in 2D Mg_3Sb_2, (h) 2D Mg_3SbBi, and (i) 2D Mg_3Bi_2.

Materials	Transferred charge	Shared charge	Transferred charge of each element		
			Mg1-site	Mg2-site	Sb/Bi-sites
Mg_3Sb_2	0.76	0.92	0.93	0.80 (0.91)	−1.47 (−1.17)
Mg_3SbBi	0.88	0.92	0.86	0.79 (0.90)	−1.17 (−1.38)
Mg_3Bi_2	0.85	0.89	0.84	0.68 (0.72)	−1.34 (−0.86)

Table 1 in the material compared to the other two structures which have higher shared electrons and stronger covalent bonding. The corresponding charges changes in the family of $Mg_3Sb_{2-x}Bi_x$ monolayers were calculated through the density-derived electrostatic and chemical (DDEC6) approach as implemented in CHARGEMOL package (Manz and Limas, 2016). Meanwhile, the higher ELF values in Mg_3Sb_2 and Mg_3SbBi monolayers also verify the higher transferred charges as seen in **Table 1** since a higher ELF usually suggests a higher concentration of localized electrons in both Mg_3Sb_2 and Mg_3SbBi compared to Mg_3Bi_2 monolayers. From **Table 1**, our analysis shows that the higher difference in electronegativity between two atoms enhances the transferred electrons which is illustrated in 2D Mg_3Sb_2 with higher difference in electronegativity between Mg and Sb atoms (higher transferred charge) compared to 2D Mg_3Bi_2 with lower difference in electronegativity between Mg and Bi atoms (lower transferred charge). On the other hand, the value of Mg-Sb atoms around the ELF distribution in 2D Mg_3SbBi is much larger when compared 2D Mg_3Sb_2 and the results is in agreement with the corresponding calculations as depicted in **Figures 4G,H**. Herein, the negative value on the abscissa represents antibonding interactions, otherwise represents bonding interactions in the three "-pCOHP" curves. Meanwhile, the absolute ICOHP (defined as $ICOHP = \int_{-\infty}^{E} pCOHP(E)dE$) serves as an indicator toward the bond strength, which can indicate the d_1 interaction trends in 2D $Mg_3Sb_{2-x}Bi_x$ (Mg_3SbBi > Mg_3Sb_2 > Mg_3Bi_2), and it is consistent with the κ_L changes. However, comparing for d_1 interactions in these compounds, we found that the absolute ICOHP for d_2 is always smaller. Typically, a weaker bond might cause phonons rattling behavior, leading the phonon modes softened, which supports the above κ_L results.

Usually, the several approaches, including the constant relaxation time approximation (Singh and Mazin, 1997; Madsen, 2006; Madsen and Singh, 2006; Yang et al., 2008), the deformation potential approximation (Sjakste et al., 2006; Murphy-Armando et al., 2010; Wang et al., 2011), and Wannier interpolation (Giustino et al., 2007; Bernardi et al., 2014; Qiu et al., 2015), can directly determine the electronic transport coefficients by solving the BTE theory. Herein, we used the EPA method to compute the corresponding parameters (S, σ, and κ_e) for the family of 2D $Mg_3Sb_{2-x}Bi_x$ compounds, which was widely verified in the previous work (Nam et al., 2021; Biele and D'Agosta, 2022). For the above compounds, we presented the variation of S versus on the values of μ at three different temperatures in **Figure 5A**. It is cleared from the figure that the maximum value of the S are 900 μV/K (Mg_3Sb_2), 750 μV/K (Mg_3SbBi), and 650 μV/K (Mg_3Bi_2) at 300 K, respectively, which are superior to those of some commercial TE materials such as SnSe (~500 μV/K) (Zhang and Zhao, 2015)and Bi_2Te_3 (~200 μV/K) (Poudel et al., 2008), suggesting the high-performance TE candidate materials for P/N-type doping 2D $Mg_3Sb_{2-x}Bi_x$. Meanwhile, there are two notable peaks around the μ–E_f value of ~0 Ry, characterizing the S curves, and the calculated S would be decreased rapidly when beyond the ranges. The negative S values of the three studied compound are smaller than that of the corresponding positive values at ~ 0 Ry region, and the discrepancy can be understood by the above band structures (mainly attributing to the band-gaps) as displayed in **Figures 4A–C**. By increasing Bi content from 2D Mg_3Sb_2 to 2D Mg_3Bi_2, the bandgap decrease gradually and thereby the absolute value of the maximum S decreases as well. As illustrated in **Figure 5B**, because of the similar electronic band structures among the three compounds, the σ curves represents a close slope at different temperatures. Moreover, we can see that the calculated σ values almost roughly increase with increasing the value of μ for all studied materials, while it is opposite for the S, indicating the two coefficients coupled unfavorably for enhancing TE performance. Furthermore, the maximum σ values for negative chemical and positive chemical potentials in the family of 2D $Mg_3Sb_{2-x}Bi_x$ compounds are almost equal at 300 K, 500 K, and 700 K.

It is well known that the trends of κ_e is tied to the σ curves, and **Figure 5C** shows the variation of κ_e with response to the μ–E_f at different temperatures. Interestingly, we can observe that the maximum values of the κ_e for negative μ region are 2.4 W/mK (2D Mg_3Sb_2), 2.6 W/mK (2D Mg_3SbBi), and 2.8 W/mK (2D Mg_3Bi_2), while for positive chemical potential region these are 1.9 W/mK (2D Mg_3Sb_2), 0.8 W/mK (2D Mg_3SbBi), and 1.6 W/mK (2D Mg_3Bi_2) at 300 K, respectively, where the calculated κ_e data is close to several commercial TE materials such as SnSe (~2 W/mK) (Wang et al., 2015) and Bi_2Te_3 (~1 W/mK) (Hicks and Dresselhaus, 1993). The results indicates that the N-type doping 2D $Mg_3Sb_{2-x}Bi_x$ composition may possess a higher TE performance compared with the corresponding P-type doping samples. Based on the phonon thermal transport and electronic transport properties computed above, we show the ZT of 2D $Mg_3Sb_{2-x}Bi_x$ compounds as a function of the μ–E_f at three typical temperatures (300 K, 500 K, and 700 K) as seen in **Figure 5D**. Obviously, the ZT in the three studied materials exhibit different trends, and the maximum ZT at 700 K can reach about 1.6 (2D Mg_3Sb_2), 0.2 (2D Mg_3SbBi), and 0.6 (2D Mg_3Bi_2), respectively. It can been clearly observed in **Figure 5D** that the TE performance of N-type doping is inferior to that of P-type doping for 2D

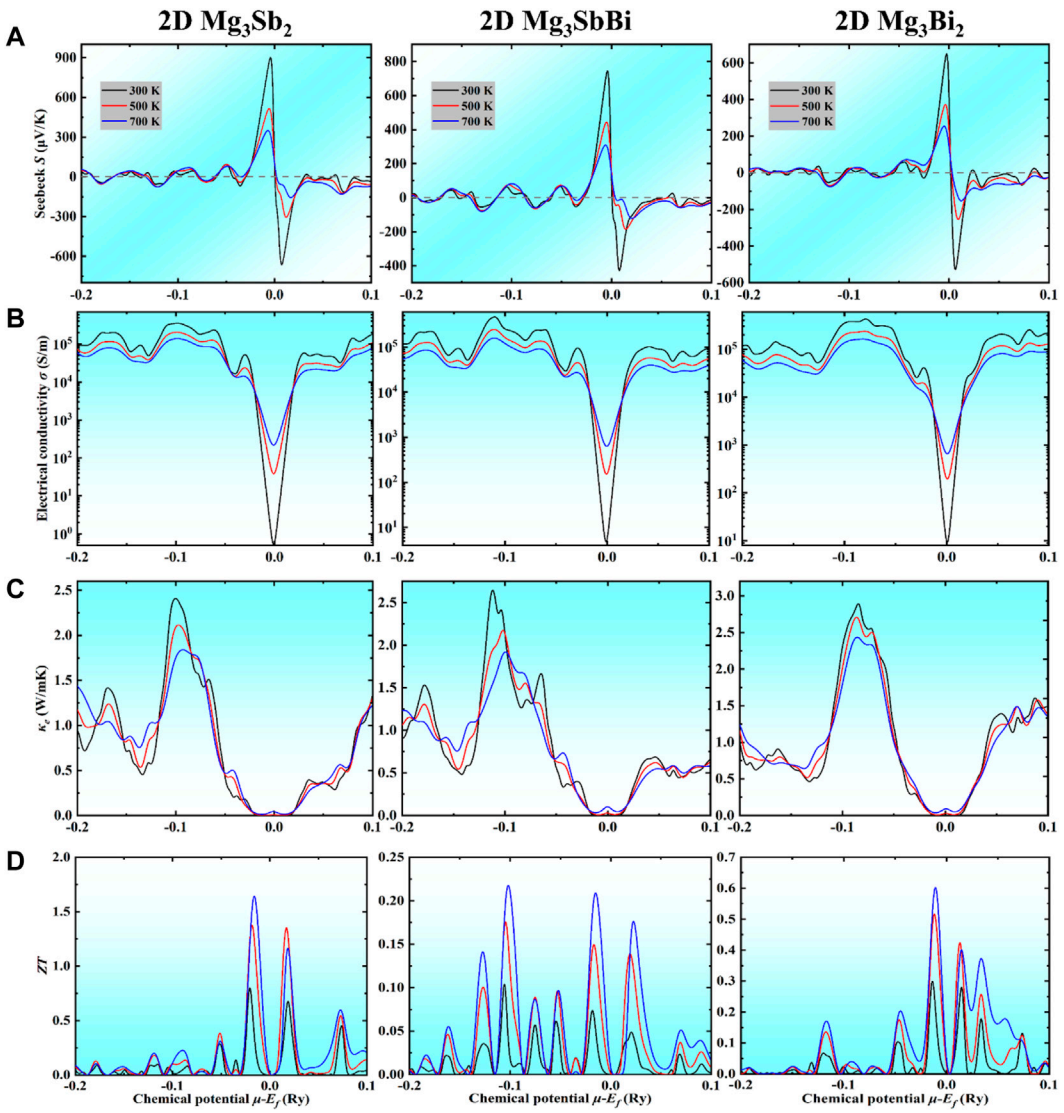

FIGURE 5 | Calculated TE transport coefficients for the 2D $Mg_3Sb_{2-x}Bi_x$ family as a function of chemical potential (μ) shifted with respect to the E_f at 300 K, 500 K, and 700 K, respectively. **(A)** Seebeck coefficient, **(B)** electrical conductivity, **(C)** electronic thermal conductivity, and **(D)** the corresponding *ZT*. Herein, the negative and positive (μ–E_f) represent the corresponding P-type and N-type samples doped, respectively.

Mg_3SbBi and 2D Mg_3Bi_2 compounds, while it is opposite for 2D Mg_3Sb_2, and the behavior has been mainly dominated by Bi element content and then changing electronic band engineering.

CONCLUSION

In summary, we have systematically investigated the TE transport properties of the family of $Mg_3Sb_{2-x}Bi_x$ (x = 0, 1, and 2) monolayers. Our results present that the three typical materials possess extremely lower lattice thermal conductivities, including 2D Mg_3Sb_2 (~0.51 W/mK), 2D Mg_3SbBi (~1.86 W/mK), and 2D Mg_3Bi_2 (~0.25 W/mK) at 300 K, respectively, while a heavier atomic mass in a compound usually possesses a lower κ_L on the basis of the conventional (Keyes' and Slack's) theory. By decomposing the κ_L, it is concluded that the abnormal phenomenon is mainly due to the effect of phonon lifetime, which is significantly larger in Mg_3SbBi alloying system. Meanwhile, all these samples exhibit a transformation from semiconductor to semimetallic with increasing Bi element content, indicating a heavier compound having a narrower band-gap. Moreover, coupling with the κ_L above, we further obtained that the maximum *ZT* values of 1.6, 0.2, and 0.6 at 700 K are founded in N-type doping 2D Mg_3Sb_2, P-type doping 2D Mg_3SbBi, and P-type doping 2D Mg_3Bi_2, respectively. All the results of the analysis above suggest that increasing Bi element to Zintl phase 2D $Mg_3Sb_{2-x}Bi_x$ alloy, which is beneficial to the reduction of the electronic thermal conduct ivies, might not necessarily improve the TE performance and offer a novel regulation approach which can be generalized in other Zintl phase monolayer compounds. Therefore, to obtain the optimal *ZT* in 2D $Mg_3Sb_{2-x}Bi_x$ alloys, both Sb and Bi element

contents (except for x = 0, 1, and 2) need be further demonstrated by coupling theoretical calculations and experimental measurements.

DATA AVAILABILITY STATEMENT

The original contributions presented in the study are included in the article/**Supplementary Material**, further inquiries can be directed to the corresponding authors.

AUTHOR CONTRIBUTIONS

ZC, JM, KY, XZ, and DT designed research. ZC: Conceptualization, Software, Formal analysis, Writing—original draft and editing, Data curation. KY, MA-F, and MH: Formal analysis, Writing—review and editing. JZ, YG, and HS performed the part calculations. All authors analyzed data and discussed results.

FUNDING

This work was supported by the National Natural Science Foundation of China [Grant Nos 51720105007, 52076031, 11602149, 51806031, 52176166) and the Fundamental Research Funds for the Central Universities [DUT19RC(3) 006], and the computing resources from the Supercomputer Center of Dalian University of Technology. Research reported in this publication was supported in part by the U.S. National Science Foundation (Award Number 1905775, 2030128).

SUPPLEMENTARY MATERIAL

The Supplementary Material for this article can be found online at: https://www.frontiersin.org/articles/10.3389/fmech.2022.876655/full#supplementary-material

REFERENCES

Bernardi, M., Vigil-Fowler, D., Lischner, J., Neaton, J. B., and Louie, S. G. (2014). Ab InitioStudy of Hot Carriers in the First Picosecond after Sunlight Absorption in Silicon. *Phys. Rev. Lett.* 112, 257402. doi:10.1103/physrevlett.112.257402

Biele, R., and D'agosta, R. (2022). Transport Coefficients of Layered TiS 3. *Phys. Rev. Mater.* 6, 014004. doi:10.1103/physrevmaterials.6.014004

Bliichl, P. (1994). Projector Augmented-Wave Method. *Phys. Rev. B* 50, 17953–17979.

Brown, S. R., Kauzlarich, S. M., Gascoin, F., and Snyder, G. J. (2006). Yb14MnSb11: New High Efficiency Thermoelectric Material for Power Generation. *Chem. Mater.* 18, 1873–1877. doi:10.1021/cm060261t

Chang, C., Wu, M., He, D., Pei, Y., Wu, C.-F., Wu, X., et al. (2018). 3D Charge and 2D Phonon Transports Leading to High Out-Of-Plane ZT in N-type SnSe Crystals. *Science* 360, 778–783. doi:10.1126/science.aaq1479

Chang, Z., Yuan, K., Sun, Z., Zhang, X., Gao, Y., Qin, G., et al. (2021). Ultralow Lattice thermal Conductivity and Dramatically Enhanced Thermoelectric Properties of Monolayer InSe Induced by an External Electric Field. *Phys. Chem. Chem. Phys.* 23, 13633–13646. doi:10.1039/d1cp01510a

Chen, X., Wu, H., Cui, J., Xiao, Y., Zhang, Y., He, J., et al. (2018). Extraordinary Thermoelectric Performance in N-type Manganese Doped Mg3Sb2 Zintl: High Band Degeneracy, Tuned Carrier Scattering Mechanism and Hierarchical Microstructure. *Nano Energy* 52, 246–255. doi:10.1016/j.nanoen.2018.07.059

Fitzgerel, R. K., and Verhoek, F. H. (1960). The Law of Dulong and Petit. . *Chem. Educ.* 37 (10), 545–549. doi:10.1021/ed037p545

Giustino, F., Cohen, M. L., and Louie, S. G. (2007). Electron-phonon Interaction Using Wannier Functions. *Phys. Rev. B* 76, 165108. doi:10.1103/physrevb.76.165108

Gorai, P., Toberer, E. S., and Stevanović, V. (2016). Computational Identification of Promising Thermoelectric Materials Among Known quasi-2D Binary Compounds. *J. Mater. Chem. A.* 4, 11110–11116. doi:10.1039/c6ta04121c

He, H., Stearrett, R., Nowak, E. R., and Bobev, S. (2010). Baga2Pn2 (Pn = P, as): New Semiconducting Phosphides and Arsenides with Layered Structures. *Inorg. Chem.* 49, 7935–7940. doi:10.1021/ic100940b

Hicks, L. D., and Dresselhaus, M. S. (1993). Effect of Quantum-Well Structures on the Thermoelectric Figure of merit. *Phys. Rev. B* 47, 12727–12731. doi:10.1103/physrevb.47.12727

Hohenberg, P., and Kohn, W. (1964). Inhomogeneous Electron Gas. *Phys. Rev.* 136, B864–B871. doi:10.1103/physrev.136.b864

Huang, S., Wang, Z., Xiong, R., Yu, H., and Shi, J. (2019). Significant Enhancement in Thermoelectric Performance of Mg3Sb2 from Bulk to Two-Dimensional Mono Layer. *Nano Energy* 62, 212–219. doi:10.1016/j.nanoen.2019.05.028

Imasato, K., Kang, S. D., Ohno, S., and Snyder, G. J. (2018). Band Engineering in Mg3Sb2 by Alloying with Mg3Bi2 for Enhanced Thermoelectric Performance. *Mater. Horiz.* 5, 59–64. doi:10.1039/c7mh00865a

Kauzlarich, S. M., Brown, S. R., and Jeffrey Snyder, G. (2007). Zintl Phases for Thermoelectric Devices. *Dalton Trans.*, 2099–2107. doi:10.1039/b702266b

Kauzlarich, S. M., Zevalkink, A., Toberer, E., and Snyder, G. J. (2016). Zintl Phases: Recent Developments in Thermoelectrics and Future Outlook.

Kresse, G., and Furthmüller, J. (1996). Efficient Iterative Schemes Forab Initiototal-Energy Calculations Using a Plane-Wave Basis Set. *Phys. Rev. B* 54, 11169–11186. doi:10.1103/physrevb.54.11169

Lee, S., Esfarjani, K., Luo, T., Zhou, J., Tian, Z., and Chen, G. (2014). Resonant Bonding Leads to Low Lattice thermal Conductivity. *Nat. Commun.* 5, 3525–3528. doi:10.1038/ncomms4525

Li, J., Liu, P.-F., Zhang, C., Shi, X., Jiang, S., Chen, W., et al. (2020a). Lattice Vibrational Modes and Phonon thermal Conductivity of Single-Layer GaGeTe. *J. Materiomics* 6, 723–728. doi:10.1016/j.jmat.2020.04.005

Li, J., Yang, J., Shi, B., Zhai, W., Zhang, C., Yan, Y., et al. (2020b). Ternary Multicomponent Ba/Mg/Si Compounds with Inherent Bonding Hierarchy and Rattling Ba Atoms toward Low Lattice thermal Conductivity. *Phys. Chem. Chem. Phys.* 22, 18556–18561. doi:10.1039/d0cp02792h

Li, W., Carrete, J., A. Katcho, N. N., and Mingo, N. (2014). ShengBTE: A Solver of the Boltzmann Transport Equation for Phonons. *Comp. Phys. Commun.* 185, 1747–1758. doi:10.1016/j.cpc.2014.02.015

Li, W., and Mingo, N. (2014). Lattice Dynamics and thermal Conductivity of Skutterudites CoSb 3 and IrSb 3 from First Principles: Why IrSb 3 Is a Better thermal Conductor Than CoSb 3. *Phys. Rev. B* 90, 094302. doi:10.1103/physrevb.90.094302

Lindsay, L., and Broido, D. A. (2008). Three-phonon Phase Space and Lattice thermal Conductivity in Semiconductors. *J. Phys. Condens. Matter* 20, 165209. doi:10.1088/0953-8984/20/16/165209

Liu, Z.-Y., Zhu, J.-L., Tong, X., Niu, S., and Zhao, W.-Y. (2020). A Review of CoSb 3-based Skutterudite Thermoelectric Materials. *J. Adv. Ceramics*, 1–27. doi:10.1007/s40145-020-0407-4

Madsen, G. K. H. (2006). Automated Search for New Thermoelectric Materials: the Case of LiZnSb. *J. Am. Chem. Soc.* 128, 12140–12146. doi:10.1021/ja062526a

Madsen, G. K. H., and Singh, D. J. (2006). BoltzTraP. A Code for Calculating Band-Structure Dependent Quantities. *Comp. Phys. Commun.* 175, 67–71. doi:10.1016/j.cpc.2006.03.007

Maintz, S., Deringer, V. L., Tchougréeff, A. L., and Dronskowski, R. (2016). *LOBSTER: A Tool to Extract Chemical Bonding from Plane-wave Based DFT*. Wiley Online Library.

Manz, T. A., and Limas, N. G. (2016). Introducing DDEC6 Atomic Population Analysis: Part 1. Charge Partitioning Theory and Methodology. *RSC Adv.* 6, 47771–47801. doi:10.1039/c6ra04656h

Murphy-Armando, F., Fagas, G., and Greer, J. C. (2010). Deformation Potentials and Electron–Phonon Coupling in Silicon Nanowires. *Nano Lett.* 10, 869–873. doi:10.1021/nl9034384

Nam, H. N., Suzuki, K., Nguyen, T. Q., Masago, A., Shinya, H., Fukushima, T., et al. (2021). *Low-temperature Acanthite-like Phase of Cu $ _ {2} $ S: A First-Principles Study on Electronic and Transport Properties. arXiv preprint arXiv:2110.09117*.

Ohno, S., Imasato, K., Anand, S., Tamaki, H., Kang, S. D., Gorai, P., et al. (2018). Phase Boundary Mapping to Obtain N-type Mg3Sb2-Based Thermoelectrics. *Joule* 2, 141–154. doi:10.1016/j.joule.2017.11.005

Okubo, K., and Tamura, S.-I. (1983). Two-phonon Density of States and Anharmonic Decay of Large-Wave-Vector LA Phonons. *Phys. Rev. B* 28, 4847–4850. doi:10.1103/physrevb.28.4847

Paier, J., Marsman, M., Hummer, K., Kresse, G., Gerber, I. C., and Ángyán, J. G. (2006). Screened Hybrid Density Functionals Applied to Solids. *J. Chem. Phys.* 124, 154709. doi:10.1063/1.2187006

Peng, B., Zhang, H., Shao, H., Xu, Y., Zhang, X., and Zhu, H. (2016). Low Lattice thermal Conductivity of Stanene. *Sci. Rep.* 6 (1), 1–10. doi:10.1038/srep20225

Perdew, J. P., Burke, K., and Ernzerhof, M. (1996). Generalized Gradient Approximation Made Simple. *Phys. Rev. Lett.* 77, 3865–3868. doi:10.1103/physrevlett.77.3865

Poudel, B., Hao, Q., Ma, Y., Lan, Y., Minnich, A., Yu, B., et al. (2008). High-thermoelectric Performance of Nanostructured Bismuth Antimony telluride Bulk Alloys. *Science* 320, 634–638. doi:10.1126/science.1156446

Qiu, B., Tian, Z., Vallabhaneni, A., Liao, B., Mendoza, J. M., Restrepo, O. D., et al. (2015). First-principles Simulation of Electron Mean-Free-Path Spectra and Thermoelectric Properties in Silicon. *Epl* 109, 57006. doi:10.1209/0295-5075/109/57006

Rowe, D. M. (2018). *Thermoelectrics Handbook: Macro to Nano*. CRC Press.

Samsonidze, G., and Kozinsky, B. (2018). Accelerated Screening of Thermoelectric Materials by First-Principles Computations of Electron-Phonon Scattering. *Adv. Energ. Mater.* 8, 1800246. doi:10.1002/aenm.201800246

Shi, X., Wang, X., Li, W., and Pei, Y. (2018). Advances in Thermoelectric Mg3Sb2and its Derivatives. *Small Methods* 2, 1800022. doi:10.1002/smtd.201800022

Shi, X., Zhang, W., Chen, L. D., and Yang, J. (2005). Filling Fraction Limit for Intrinsic Voids in Crystals: Doping in Skutterudites. *Phys. Rev. Lett.* 95, 185503. doi:10.1103/physrevlett.95.185503

Shu, R., Zhou, Y., Wang, Q., Han, Z., Zhu, Y., Liu, Y., et al. (2019). Mg3+ δ Sb X Bi2− X Family: A Promising Substitute for the State-Of-The-Art N-type Thermoelectric Materials Near Room Temperature. *Adv. Funct. Mater.* 29, 1807235. doi:10.1002/adfm.201807235

Shuai, J., Mao, J., Song, S., Zhang, Q., Chen, G., and Ren, Z. (2017). Recent Progress and Future Challenges on Thermoelectric Zintl Materials. *Mater. Today Phys.* 1, 74–95. doi:10.1016/j.mtphys.2017.06.003

Silvi, B., and Savin, A. (1994). Classification of Chemical Bonds Based on Topological Analysis of Electron Localization Functions. *Nature* 371, 683–686. doi:10.1038/371683a0

Singh, D. J., and Mazin, I. I. (1997). Calculated Thermoelectric Properties of La-Filled Skutterudites. *Phys. Rev. B* 56, R1650–R1653. doi:10.1103/physrevb.56.r1650

Sjakste, J., Tyuterev, V., and Vast, N. (2006). Ab Initiostudy ofΓ–Xintervalley Scattering in GaAs under Pressure. *Phys. Rev. B* 74, 235216. doi:10.1103/physrevb.74.235216

Sun, X., Li, X., Yang, J., Xi, J., Nelson, R., Ertural, C., et al. (2019). Achieving Band Convergence by Tuning the Bonding Ionicity in N-type Mg 3 Sb 2. *J. Comput. Chem.* 40, 1693–1700. doi:10.1002/jcc.25822

Wang, F. Q., Zhang, S., Yu, J., and Wang, Q. (2015). Thermoelectric Properties of Single-Layered SnSe Sheet. *Nanoscale* 7, 15962–15970. doi:10.1039/c5nr03813h

Wang, J., Xia, S.-Q., and Tao, X.-T. (2012). A5Sn2As6 (A = Sr, Eu). Synthesis, Crystal and Electronic Structure, and Thermoelectric Properties. *Inorg. Chem.* 51, 5771–5778. doi:10.1021/ic300308w

Wang, Z., Wang, S., Obukhov, S., Vast, N., Sjakste, J., Tyuterev, V., et al. (2011). Thermoelectric Transport Properties of Silicon: Toward Anab Initioapproach. *Phys. Rev. B* 83, 205208. doi:10.1103/physrevb.83.205208

Wood, M., Imasato, K., Anand, S., Yang, J., and Snyder, G. J. (2020). The Importance of the Mg-Mg Interaction in Mg3Sb2-Mg3Bi2 Shown through Cation Site Alloying. *J. Mater. Chem. A.* 8, 2033–2038. doi:10.1039/c9ta11328b

Wu, Y., Ma, C., Chen, Y., Mortazavi, B., Lu, Z., Zhang, X., et al. (2020). New Group V Graphyne: Two-Dimensional Direct Semiconductors with Remarkable Carrier Mobilities, Thermoelectric Performance, and thermal Stability. *Mater. Today Phys.* 12, 100164. doi:10.1016/j.mtphys.2019.100164

Xia, S.-Q., and Bobev, S. (2007). Cation−Anion Interactions as Structure Directing Factors: Structure and Bonding of Ca2CdSb2 and Yb2CdSb2. *J. Am. Chem. Soc.* 129, 4049–4057. doi:10.1021/ja069261k

Xin, J., Li, G., Auffermann, G., Borrmann, H., Schnelle, W., Gooth, J., et al. (2018). Growth and Transport Properties of Mg3X2 (X = Sb, Bi) Single Crystals. *Mater. Today Phys.* 7, 61–68. doi:10.1016/j.mtphys.2018.11.004

Yang, J., Li, H., Wu, T., Zhang, W., Chen, L., and Yang, J. (2008). Evaluation of Half-Heusler Compounds as Thermoelectric Materials Based on the Calculated Electrical Transport Properties. *Adv. Funct. Mater.* 18, 2880–2888. doi:10.1002/adfm.200701369

Yang, Z., Yuan, K., Meng, J., Zhang, X., Tang, D., and Hu, M. (2020). Why thermal Conductivity of CaO Is Lower Than that of CaS: a Study from the Perspective of Phonon Splitting of Optical Mode. *Nanotechnology* 32, 025709. doi:10.1088/1361-6528/abbb4c

Yue, S.-Y., Qin, G., Zhang, X., Sheng, X., Su, G., and Hu, M. (2017). Thermal Transport in Novel Carbon Allotropes with S P 2 or S P 3 Hybridization: An Ab Initio Study. *Phys. Rev. B* 95, 085207. doi:10.1103/physrevb.95.085207

Zeng, J., He, X., Liang, S.-J., Liu, E., Sun, Y., Pan, C., et al. (2018). Experimental Identification of Critical Condition for Drastically Enhancing Thermoelectric Power Factor of Two-Dimensional Layered Materials. *Nano Lett.* 18, 7538–7545. doi:10.1021/acs.nanolett.8b03026

Zevalkink, A., Pomrehn, G., Takagiwa, Y., Swallow, J., and Snyder, G. J. (2013). Thermoelectric Properties and Electronic Structure of the Zintl-phase Sr3AlSb3. *ChemSusChem* 6, 2316–2321. doi:10.1002/cssc.201300518

Zevalkink, A., Zeier, W. G., Pomrehn, G., Schechtel, E., Tremel, W., and Snyder, G. J. (2012). Thermoelectric Properties of Sr3GaSb3 - a Chain-Forming Zintl Compound. *Energy Environ. Sci.* 5, 9121–9128. doi:10.1039/c2ee22378c

Zhang, J., Song, L., Sist, M., Tolborg, K., and Iversen, B. B. (2018). Chemical Bonding Origin of the Unexpected Isotropic Physical Properties in Thermoelectric Mg3Sb2 and Related Materials. *Nat. Commun.* 9 (1), 1–10. doi:10.1038/s41467-018-06980-x

Zhang, J., and Iversen, B. B. (2019). Fermi Surface Complexity, Effective Mass, and Conduction Band Alignment in N-type Thermoelectric Mg3Sb2 - xBix from First Principles Calculations. *J. Appl. Phys.* 126, 085104. doi:10.1063/1.5107484

Zhang, J., Song, L., and Iversen, B. B. (2019). Insights into the Design of Thermoelectric Mg3Sb2 and its Analogs by Combining Theory and experiment. *npj Comput. Mater.* 5, 1–17. doi:10.1038/s41524-019-0215-y

Zhang, X., and Zhao, L.-D. (2015). Thermoelectric Materials: Energy Conversion between Heat and Electricity. *J. Materiomics* 1, 92–105. doi:10.1016/j.jmat.2015.01.001

Zhao, L.-D., Lo, S.-H., Zhang, Y., Sun, H., Tan, G., Uher, C., et al. (2014). Ultralow thermal Conductivity and High Thermoelectric Figure of merit in SnSe Crystals. *Nature* 508, 373–377. doi:10.1038/nature13184

Zhao, L.-D., Tan, G., Hao, S., He, J., Pei, Y., Chi, H., et al. (2016). Ultrahigh Power Factor and Thermoelectric Performance in Hole-Doped Single-crystal SnSe. *Science* 351, 141–144. doi:10.1126/science.aad3749

Conflict of Interest: The authors declare that the research was conducted in the absence of any commercial or financial relationships that could be construed as a potential conflict of interest.

Publisher's Note: All claims expressed in this article are solely those of the authors and do not necessarily represent those of their affiliated organizations, or those of the publisher, the editors and the reviewers. Any product that may be evaluated in this article, or claim that may be made by its manufacturer, is not guaranteed or endorsed by the publisher.